

Polarization–Magnetization Coupling in Visible-Light Ferroelectric Double Perovskites

Sathiyamoorthy Buvaneswaran,¹ Trilochan Sahoo,¹ and Saurabh Ghosh^{1,2,*}

¹*Department of Physics and Nanotechnology, Faculty of Engineering and Technology, SRM Institute of Science and Technology, Kattankulathur 603 203, Tamil Nadu, India*

²*Center for Advanced Computational and Theoretical Sciences (SRM-ACTS), Faculty of Engineering and Technology, SRM Institute of Science and Technology, Kattankulathur 603 203, Tamil Nadu, India*

(Dated: November 11, 2025)

The bulk photovoltaic effect (BPVE), arising from broken inversion symmetry in ferroelectrics, offers a distinct pathway toward high-efficiency next-generation photovoltaics. We propose and investigate A/A'-ordered double perovskites KLaFeMoO₆ and NaLaFeMoO₆ as promising single-phase ferroelectric photovoltaic (FE-PV) materials. First-principles calculations reveal robust $P2_1$ symmetry with A-site layer and B-site rock-salt ordering, accompanied by hybrid improper ferroelectricity driven by $a^-a^-c^+$ octahedral tilts. Both compounds exhibit significant spontaneous polarization and indirect band gaps of ~ 1.8 eV, well suited for visible-light absorption ($>10^5$ cm⁻¹). Low carrier effective masses along the polar axis indicate efficient charge transport. *Ab initio* molecular dynamics simulations (AIMD) show that polarization-coupled magnetization switching is feasible above room temperature, making these materials suitable for room-temperature applications.

The BPVE, which arises in noncentrosymmetric single-phase materials, enables the generation of photocurrent without requiring a p–n junction [1–3]. In such polar systems, the intrinsic electric field associated with spontaneous polarization facilitates the separation of photoexcited electron–hole pairs. Unlike conventional photovoltaic mechanisms, BPVE can yield open-circuit voltages exceeding the electronic band gap [4, 5], offering a potential route to surpass the Shockley–Queisser limit [6]. Ferroelectric perovskites such as BaTiO₃, LiNbO₃, and Pb(Zr,Ti)O₃, etc., have been extensively studied in this context [7–10]; however, their wide band gaps > 3 eV limit absorption to the ultraviolet region, thus constraining their photovoltaic performance. Among them, BiFeO₃ has attracted particular attention due to its large spontaneous polarization and high Curie temperature (T_c), but its relatively large bandgap (~ 2.67 eV) and weak absorption in the visible range lead to limited photocurrent generation in practical applications [11–13]. These limitations highlight the need for novel ferroelectric materials that combine large polarization, an appropriate bandgap, strong visible-light absorption, efficient charge-transport characteristics, and robust ferroelectricity sustained at or above room temperature.

Double perovskite oxides (DPOs), with the chemical formula AA'BB'O₆, are promising candidates in this context. Their structural and functional properties in DPOs are governed by collective lattice distortions and symmetry-breaking couplings among key modes—namely, in-phase (Q_{R+} , $a^0a^0c^+$) and out-of-phase (Q_{R-} , $a^0a^0c^-$) octahedral rotations, in-plane tilts (Q_T , $a^-a^-c^0$), and polar A-site displacements (Q_{AFEA}) [14–16]. The most common cation configuration features rock-salt ([R]) ordering on the B/B' sublattice and layered ([L]) or rock-salt ordering on the A/A' sublattice. When A-site [L] and B-site [R] orderings coexist with an $a^-a^-c^+$ tilt pattern, the lattice symmetry is reduced to a polar $P2_1$ phase. This symmetry breaking is driven by a trilinear coupling between the nonpolar Q_T and Q_{R+} modes and the polar Q_{AFEA} mode—characteristic of hybrid improper ferroelectricity (HIF). Thus, identifying DPOs with

stable AA'-site ordering, strong spontaneous polarization, and reduced bandgap opens up avenues to design novel visible-light-absorbing FE-PV materials.

In this work, we investigate KLaFeMoO₆ and NaLaFeMoO₆ DPOs as promising FE-PV materials capable of operating at or above room temperature. DFT calculations reveal a polar $P2_1$ ground state with A-site [L] and B-site [R] ordering and an $a^-a^-c^+$ octahedral tilt pattern. Phonon symmetry-mode analysis identifies three key distortion modes (Q_{R+} , Q_T , Q_{AFEA}) that drive inversion symmetry breaking via the HIF mechanism, yielding robust polarization along the b -axis. Electronic structure calculations reveal indirect band gaps in the optimal ~ 1.8 eV range, strong visible-light absorption ($>10^5$ cm⁻¹), and low carrier effective masses along the polar b axis, favorable for carrier mobility. AIMD simulations show that the polarization coupled magnetization switching exceeds room temperature, confirming the thermal stability and suitability of the compounds for room-temperature multiferroic and optoelectronic applications. We have discussed how behaviour of the real part of the dielectric function can detect polarization-coupled magnetization switching.

Computational details: First-principles density functional theory (DFT) calculations [17, 18] were performed using the full-potential linearized augmented plane wave (FP-LAPW) method in the WIEN2k package [19]. Structural relaxations employed the GGA-PBE functional [20] with a Γ -centered $6 \times 6 \times 4$ k -point mesh. On-site Coulomb interactions for transition metal d orbitals were treated via the GGA+ U scheme with Hubbard parameter $U_{\text{eff}} = U - J_H$ of 4.5 eV for Fe (3d) and 1.0 eV for Mo (4d)[21]. Electronic structure and band gaps were further refined using the Modified Becke–Johnson (MBJ) potential [22] with spin-orbit coupling (SOC) along all three crystallographic directions, considering the low-spin configurations along the b -axis. Geometry optimizations were converged when the total energy change was below 10^{-8} eV and Hellmann–Feynman forces were below 0.001 eV Å⁻¹. Electronic and optical properties were computed using

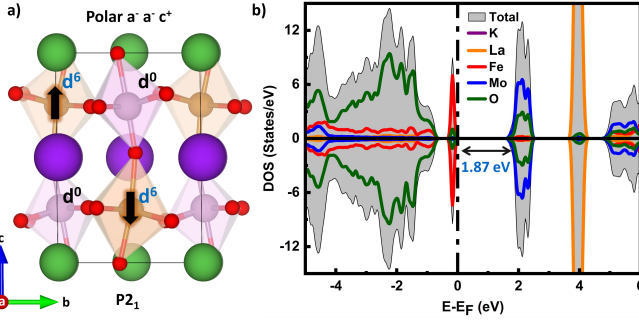


FIG. 1. Optimized $P2_1$ structure of KLaFeMoO_6 showing A-type AFM ordering, in which Fe spins are ferromagnetically aligned within the ab plane and antiferromagnetically coupled along the c axis. (b) Corresponding total DOS of KLaFeMoO_6 .

GGA+U+MBJ+SOC on a $12 \times 12 \times 8$ k -point mesh. The reliability of this approach for similar systems has been validated in our previous studies [23, 24].

Origin of ferroelectricity: The compound $\text{Sr}_2\text{FeMoO}_6$ (SFMO) in the tetragonal $I4/mmm$ phase is a well-known half-metallic ferromagnet, exhibiting robust Fe/Mo rock-salt ordering and a high T_c (≈ 410 – 450 K) [25, 26]. In this phase, Fe^{3+} ($S = 5/2$) and Mo^{5+} ($S = 1/2$) sublattices are ferromagnetically aligned within their own sublattice, while the two sublattices are antiferromagnetically coupled to each other [27, 28]. These features make SFMO a benchmark system in spintronics and an excellent electronic platform for designing multifunctional materials. The optimized structure with spin configuration and the calculated density of states (DOS) of SFMO, consistent with earlier reports [29–31], are shown in Fig. S1 of the Supplemental Material (SM) [32]. We select K^{1+} and La^{3+} at the (A, A')-site to replace Sr^{2+} on this SFMO parent structure. Our previous studies indicated that the large charge and size contrast between A and A' promotes strong A-site cation ordering, which is essential for stabilizing polar distortions and enabling HIF in DPOs [33].

To induce ferroelectricity in DPOs, two key structural conditions must be satisfied: (i) stabilization of the $a^-a^-c^+$ tilt pattern within the polar $P2_1$ phase and (ii) formation of A/A'-site layered ordering. The $a^-a^-c^+$ tilt configuration breaks inversion symmetry, while the A/A' cation ordering further couples with octahedral rotations to generate spontaneous polarization via the HIF mechanism. DFT total energy calculations confirm that the $P2_1$ phase with an $a^-a^-c^+$ tilt pattern is the most stable configuration among various possible tilt distortions. To evaluate cation ordering tendencies, special quasi-random structure (SQS) models [34] were employed, which reveal that the ordered arrangement is energetically more favorable than disordered configurations. Combined DFT and SQS results thus confirm that KLaFeMoO_6 stabilizes in a polar $P2_1$ phase with an $a^-a^-c^+$ tilt pattern and A-site [L] and B-site [R] ordering. A detailed explanation of the SQS calculation method and results is provided in SM Note S1 [32].

To elucidate the origin of ferroelectricity in KLaFeMoO_6 , we performed functional mode analysis by decomposing the low-symmetry polar $P2_1$ structure with respect to the high-symmetry cubic $P4/nmm$ reference phase (SM Fig. S3 (a,b)). Phonon mode decomposition identifies four dominant lattice distortions: in-plane octahedral tilting (Q_T), out-of-plane rotation (Q_{R+}), two-dimensional charge disproportionation ($Q_{\text{CD}2\text{D}}$), and polar A-site displacement (Q_{AFEA}), as illustrated in SM Fig. S3 (c–f) [32]. The corresponding group-subgroup relationship further outlines the symmetry-lowering pathway through several intermediate phases, as depicted in SM Fig. S3 (g) [32]. A trilinear coupling among the Q_T , Q_{R+} , and Q_{AFEA} modes stabilizes the ferroelectric $P2_1$ phase through a HIF mechanism, resulting in a polarization along the b axis (\vec{P}_y). The calculated \vec{P}_y of KLaFeMoO_6 is $\sim 14.42 \mu\text{C}/\text{cm}^2$ using the Berry phase method [35].

In the ground state, Fe ions are in the $2+$ oxidation state with a high-spin $3d^6$ configuration ($\text{Fe}^{2+} : t_{2g}^4 e_g^2$, $S = 2$), while Mo ions adopt a $6+$ oxidation state corresponding to an empty $4d^0$ configuration ($\text{Mo}^{6+} : t_{2g}^0 e_g^0$, $S = 0$). To identify the magnetic ground state of KLaFeMoO_6 we compared the total energies of different magnetic orderings, including ferromagnetic (FM) and A-, C-, and G-type antiferromagnetic (AFM) configurations. The lowest-energy state corresponds to A-type AFM ordering, in which Fe moments align ferromagnetically within the ab -plane and couple antiferromagnetically along the c -axis as shown in Fig. 1a. In this configuration, Fe exhibits a strong spin moment ($3.73 \mu_B/\text{Fe}^{2+}$) and Mo develops a weaker spin moment ($0.03 \mu_B/\text{Mo}^{6+}$) due to exchange-induced polarization effect.

To further explore the effect of A-site substitution, we replaced K with Na in the KLaFeMoO_6 lattice. The resulting NaLaFeMoO_6 stabilizes in the same polar $P2_1$ ($a^-a^-c^+$). The calculated polarization increases to $\sim 21.32 \mu\text{C}/\text{cm}^2$ (with full path polarization calculation), attributed to the smaller ionic radius mismatch between Na^{1+} and La^{3+} . It also retains A-type AFM ordering, with Fe and Mo magnetic moments slightly modified due to changes in the Fe–O–Mo bond angle and bond length. The optimized structure and corresponding DOS are shown in Fig. S4. The structural and magnetic parameters are compared in Table S1 [32].

Electronic structure and band dispersion: From the above studies, we confirm that both materials exhibit strong ferroelectric polarization, which facilitates efficient separation of photoexcited carriers. The DOS profile of KLaFeMoO_6 , as depicted in Fig. 1b, reveals that the valence band (VB) is primarily governed by strong Fe- $3d$ and O- $2p$ hybridization, while the conduction band (CB) mainly originates from overlapping Mo- $4d$ and O- $2p$ states. Such transition-metal–oxygen hybridization promotes delocalized electronic states, thereby enhancing carrier mobility and reducing recombination. The electronic structure indicates that KLaFeMoO_6 is an indirect band-gap semiconductor with an energy gap of 1.87 eV. Although an indirect band gap is less favorable for light absorption, it can reduce radiative electron–hole recombination rate, leading to longer carrier life-

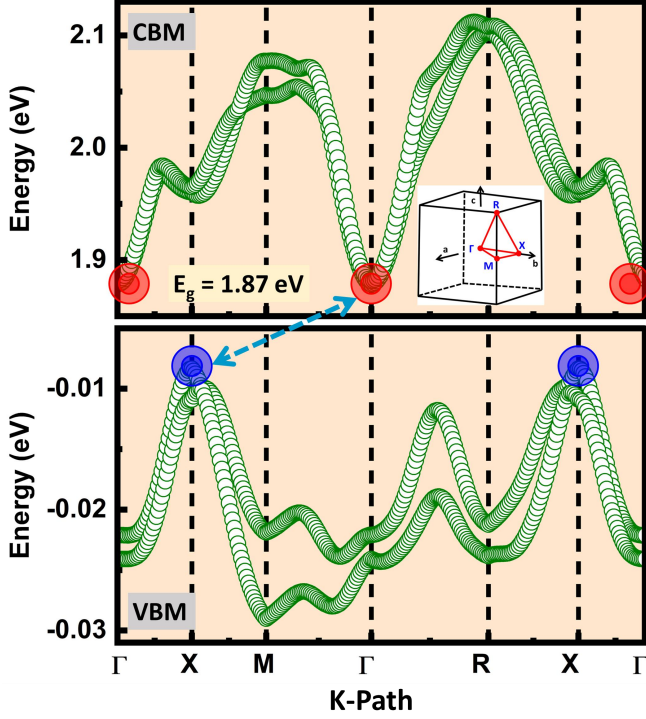


FIG. 2. Band dispersion of the highest VB and the lowest CB along high-symmetry directions in the Brillouin zone of KLaFeMoO₆, calculated using GGA+U+MBJ+SOC. Blue and red circles indicate the maxima of VB and minima of CB, respectively.

TABLE I. Calculated hole (m_h^*) and electron (m_e^*) effective masses (in units of electron mass m_e) for AA'FeMoO₆ (AA' = KLa and NaLa) along different high-symmetry directions.

| Direction | m_e^* | | Direction | m_h^* | |
|-----------|---------|------|-----------|---------|------|
| | KLa | NaLa | | KLa | NaLa |
| X-Γ-X | 0.55 | 0.63 | Γ-X-Γ | 1.91 | 1.98 |
| M-Γ-M | 0.59 | 0.68 | M-X-M | 2.53 | 2.61 |
| R-Γ-R | 0.64 | 0.71 | R-X-R | 2.83 | 2.93 |

times (τ) and greater diffusion lengths [36]. The strong Fe–O and Mo–O covalency near the Fermi level in the VB and CB produces a high density of states, which can enhance optical transitions, increase the absorption coefficient in the visible region, and thereby boost photocurrent generation. Similarly, DOS profile of NaLaFeMoO₆, as shown in SM Fig. S4b [32], displays an indirect band gap of 1.82 eV, indicating that A-site chemistry has minimal influence on the energy gap since A-site states lie far from the Fermi level. The slight variation arises from subtle modifications in Fe–O–Mo bond geometry, consistent with earlier reports [23, 24].

The band dispersion of the highest VB and lowest CB of KLaFeMoO₆, calculated using GGA+U+MBJ+SOC, is shown in Fig. 2. The band gap separates states formed by hybridized Fe-3d/O-2p (VB) and Mo-4d/O-2p (CB) orbitals, both exhibiting significant dispersion near the Fermi level, indicative of low carrier effective masses (m^*). Such dispersive

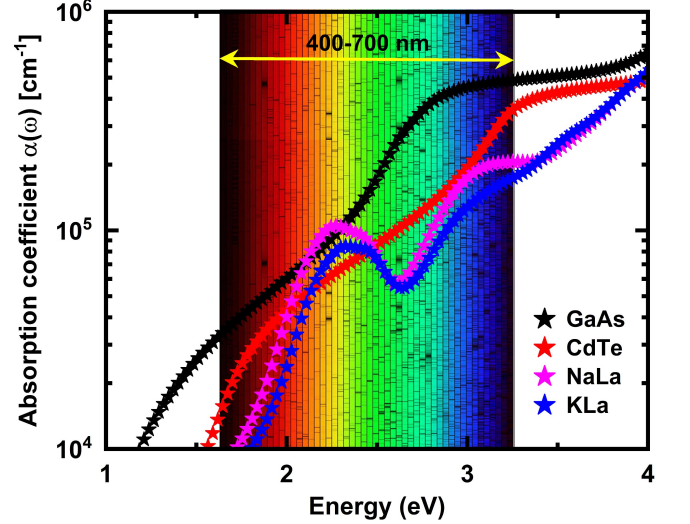


FIG. 3. Calculated optical absorption spectrum $\alpha(\omega)$ of AA'FeMoO₆ (AA' = KLa and NaLa), compared with conventional semiconductors GaAs and CdTe.

features are beneficial for charge transport, as carrier mobility $\mu \propto 1/m^*$. The band structure of NaLaFeMoO₆ is provided in SM Fig. S5 [32]. To quantify these features, we calculated the m^* value of both NaLaFeMoO₆ and KLaFeMoO₆ along different high-symmetry directions in the Brillouin zone (inserted in Fig. 2), with the values summarized in Table I.

The electron (m_e^*) and hole (m_h^*) effective masses were obtained from the curvature of the CB minimum (Red circle) and VB maximum (Blue circle), respectively, as indicated in the band dispersion plot. These values are comparable to those of well-known BPVE materials, including BiFeO₃ ($m_e^* = 0.691 m_e$, $m_h^* = 3.171 m_e$), KNbO₃ ($m_e^* = 1.559 m_e$, $m_h^* = 2.743 m_e$), and tetragonal BaTiO₃ ($m_e^* = 0.482 m_e$, $m_h^* = 1.082 m_e$). This comparison highlights that both NaLaFeMoO₆ and KLaFeMoO₆ possess carrier transport characteristics on par with well established BPVE systems. Notably, the lowest effective masses were found along the polar b-axis (X-Γ-X), a direction of particular importance since previous experiments have shown that photo-induced output voltage V_{OC} is observed only along the polarization axis (Perpendicular to the domain wall) [4]. Thus, the combination of anisotropic band dispersion and low effective masses strongly suggests that these compounds are highly promising for efficient FE-PV applications.

To assess the optical response and light-harvesting potential, the absorption coefficient $\alpha(\omega)$ was calculated from the frequency-dependent complex dielectric function as depicted in Fig. 3. The $\alpha(\omega)$ spectra of KLaFeMoO₆ and NaLaFeMoO₆ show sharp optical onsets at 1.87 eV and 1.82 eV, respectively, positioning them in the optimal range for visible-light harvesting, superior to well-known BPVE material BiFeO₃ [12, 37], and comparable with traditional PV semiconductors like GaAs and CdTe [38–40], as shown in Fig. 3. Above 2 eV, both materials exhibit $\alpha(\omega)$ value exceeding

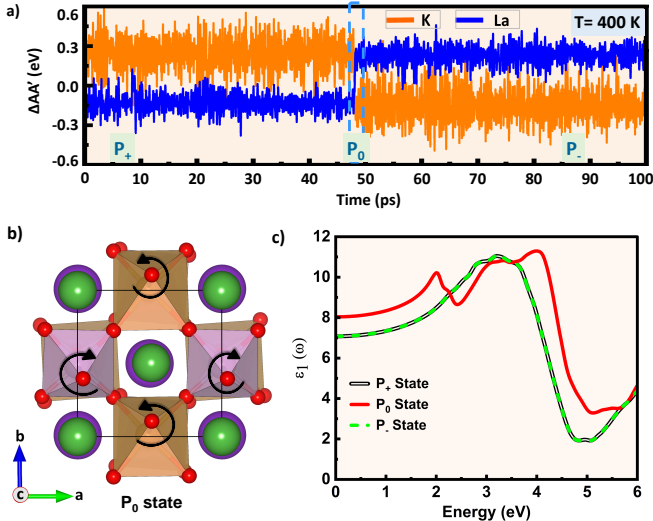


FIG. 4. (a) Displacement of K and La atoms over 100 ps at 400 K. Snapshot of the structure in the intermediate polarization state (\vec{P}_0). (c) Real part of the dielectric function $\epsilon_1(\omega)$ for the polarization states (P_+), (P_0) and (P_-).

$1 \times 10^5 \text{ cm}^{-1}$, ensuring strong light-matter interaction and efficient electron-hole generation. The redshift and increased $\alpha(\omega)$ observed in NaLaFeMoO₆ relative to KLaFeMoO₆ are attributed to its smaller band gap and high DOS of hybridized Fe-O in VB and Mo-O states in CB near the Fermi level (Refer SM Fig. S4b). In both materials, the first sharp absorption peak arises from transitions between these strongly coupled states. This combination of strong visible-light absorption and spontaneous polarization facilitates high photocurrent generation together with efficient BPVE-driven carrier separation, highlighting their potential for FE-PV devices.

Ferroelectric operating temperature (T_S): The above studies have highlighted the potential of these materials as single-phase FE-PV candidates. However, for practical applications, stability of the FE phase at or above room temperature is essential to sustain polarization and ensure a steady photocurrent. If polarization becomes unstable or reverses spontaneously, persistent photocurrent cannot be maintained [41]. To identify the temperature range over which polarization remains stable, we assessed the ferroelectric operating temperature (T_S) using ab-initio molecular dynamics (AIMD) simulations. A $2 \times 2 \times 2$ (160-atom) supercell of NaLaFeMoO₆ and KLaFeMoO₆ was used and the displacement of A (K and Na) and A' (La) cations from their centrosymmetric positions $\Delta A A'$ (Å), as a function of time steps Δt (ps) at different temperatures was recorded during the simulations, are presented in Fig. S6 and S7 of the SM [32].

For the KLaFeMoO₆ system, at 300 K, A(K) and A'(La) site cations exhibit displacements, and the corresponding structure remains in the polar P_{21} phase with the $a^-a^-c^+$ tilt pattern and polarization \vec{P}_y aligned along [010] (\vec{P}_+ state). When the temperature is increased to 400 K, the system initially retains the \vec{P}_+ state. However, around 48 ps, the K and

La cations acquire sufficient thermal energy to overcome the potential barrier and shift their positions as shown in the Fig. 4a. Structural analysis in the 48–100 ps window shows that the system still belongs to the P_{21} phase but adopts a different tilt pattern $a^-a^-(-c)^+$, in which the entire in-phase tilt pattern reverses from $a^-a^-c^+$ to $a^-a^-(-c)^+$ along the c axis. This transition confirms polarization switching in rotationally induced HIF materials [42, 43]. Specifically, the polarization switches from [010] (\vec{P}_+ state) to [0 $\bar{1}$ 0] (\vec{P}_- state) at 400 K (~ 48 ps). Fig. S8 of the SM [32] shows snapshots of the \vec{P}_+ , \vec{P}_0 , and \vec{P}_- states. The \vec{P}_0 state preserves the tilt but loses the in-phase rotation, leading to negligible AA'-cation displacements as shown in Fig. 4b. In the case of NaLaFeMoO₆, polarization switching occurs at 700 K, indicating a significantly higher T_S . This behavior arises from the smaller ionic radius mismatch between Na and La, which reduces A-site off-centering and thereby increases the energy barrier for polarization reversal, consistent with previous reports [23, 24].

Switching pathway: To gain insight into the microscopic switching mechanism, we analyzed the structural evolution of KLaFeMoO₆ during polarization reversal. The system initially adopts the in-phase tilt configuration ($a^-a^-c^+$), with anti-phase octahedral tilts along the a - and b -axes and an in-phase tilt along the c -axis. Simultaneously, the octahedra exhibit an in-phase rotation around the c -axis ($a^0a^0c^+$), which stabilizes the initial polarization and magnetization. During switching, the structure evolves toward the out-of-phase tilt configuration ($a^-a^-c^0$), retaining the anti-phase tilts along a and b but losing the c -axis tilt. Remarkably, the in-phase rotation ($a^0a^0c^+$) persists, maintaining a finite rotational component that stabilizes the system. This mode of switching, in which the tilt gradually changes from in-phase to out-of-phase while the in-phase rotation remains unchanged, is referred to as tilt precession Q_{Tp} [44]. A snapshot of this pathway is provided in Fig. S8 of the SM [32]. The persistence of Q_{R+} coupled with Q_{Tp} plays a critical role in stabilizing both the polarization and magnetization vectors, ensuring an energetically favorable transition. As shown in Fig. 4a, around 48 ps, not only polarization switches, but also polarization-coupled magnetization switching is observed. A noncollinear configuration characterized by $F_x A_y G_z$ shows reversal of the weak ferromagnetic component along x ($+F_x \rightarrow -F_x$, with magnetization along x , $m_x = 0.35 \mu_B/\text{Fe}$ driven by polarization reversal ($+P_y \rightarrow -P_y$, with polarization along $P_y = 21.32 \mu\text{C}/\text{cm}^2$).

The dielectric response, shown in Fig. 4c, provides an additional probe to track polarization switching. At 400 K, both the P_+ (0–48 ps) and P_- (48–100 ps) states exhibit nearly identical $\epsilon_1(\omega)$ spectra, with a static dielectric constant of 7.07, indicating that the reversal of octahedral tilt orientation alone does not significantly affect the optical response. In contrast, the transient P_0 state (~ 48 ps) shows a clear enhancement, with the static dielectric constant increasing to 8.03. This enhancement results from the suppression of in-phase rotation, which eliminates ionic polarization but strengthens

Fe–O/Mo–O orbital overlap. The resulting band-gap narrowing increases the joint DOS near the band edges, thereby amplifying optical transitions. Thus, the dielectric spectrum not only reflects electronic structure changes but also serves as a reliable indicator of polarization switching, revealing the strong coupling between polarization dynamics, band structure, and dielectric response.

In conclusion, we proposed and characterized A/A'-ordered double perovskites KLaFeMoO₆ and NaLaFeMoO₆ as promising single-phase ferroelectric photovoltaics. They exhibit A-site [L] and B-site [R] ordering with P2₁ symmetry, $a^-a^-c^+$ tilts, and significant polarization. Both compounds have indirect band gaps (1.87 and 1.82 eV), strong visible-light absorption ($>10^5$ cm⁻¹), and low effective masses along the polar axis, favorable for efficient charge transport. AIMD simulations confirm that both materials maintain a stable ferroelectric phase at or above room temperature, with tilt-precession as the primary pathway for polarization and magnetization reversal. These results highlight their potential for next-generation ferroelectric photovoltaic and multifunctional optoelectronic applications.

S.G. acknowledges funding from DST-ANRF Core Research Grant File. no. CRG/2023/3209 for funding. S.B. acknowledges the SRMIST KTR for his fellowship.

* saurabhghosh2802@gmail.com

- [1] W. Kraut and R. von Baltz, Anomalous bulk photovoltaic effect in ferroelectrics: a quadratic response theory, *Physical Review B* **19**, 1548 (1979).
- [2] R. von Baltz and W. Kraut, Theory of the bulk photovoltaic effect in pure crystals, *Physical Review B* **23**, 5590 (1981).
- [3] A. Bhatnagar, A. Roy Chaudhuri, Y. Heon Kim, D. Hesse, and M. Alexe, Role of domain walls in the abnormal photovoltaic effect in bifeo₃, *Nature communications* **4**, 2835 (2013).
- [4] S. Yang, J. Seidel, S. Byrnes, P. Shafer, C.-H. Yang, M. Rossell, P. Yu, Y.-H. Chu, J. Scott, J. Ager, *et al.*, Above-bandgap voltages from ferroelectric photovoltaic devices, *Nature nanotechnology* **5**, 143 (2010).
- [5] J. Seidel, D. Fu, S.-Y. Yang, E. Alarcón-Lladó, J. Wu, R. Ramesh, and J. W. Ager III, Efficient photovoltaic current generation at ferroelectric domain walls, *Physical review letters* **107**, 126805 (2011).
- [6] J. E. Spanier, V. M. Fridkin, A. M. Rappe, A. R. Akbashev, A. Polemi, Y. Qi, Z. Gu, S. M. Young, C. J. Hawley, D. Imbrenda, *et al.*, Power conversion efficiency exceeding the shockley–queisser limit in a ferroelectric insulator, *Nature Photonics* **10**, 611 (2016).
- [7] M. Ichiki, R. Maeda, Y. Morikawa, Y. Mabune, T. Nakada, and K. Nonaka, Photovoltaic effect of lead lanthanum zirconate titanate in a layered film structure design, *Applied Physics Letters* **84**, 395 (2004).
- [8] V. M. Fridkin and B. Popov, Anomalous photovoltaic effect in ferroelectrics, *Soviet Physics Uspekhi* **21**, 981 (1978).
- [9] A. Glass, D. v. d. Linde, and T. Negran, High-voltage bulk photovoltaic effect and the photorefractive process in linbo₃, in *Landmark Papers On Photorefractive Nonlinear Optics* (World Scientific, Singapore, 1995) pp. 371–373.
- [10] E. Dubovik, V. Fridkin, and D. Dimos, The bulk photovoltaic effect in ferroelectric pb (zr, ti) o₃ thin films, *Integrated Ferroelectrics* **8**, 285 (1995).
- [11] T. Choi, S. Lee, Y. Choi, V. Kiryukhin, and S.-W. Cheong, Switchable ferroelectric diode and photovoltaic effect in bifeo₃, *Science* **324**, 63 (2009).
- [12] S. Basu, L. Martin, Y. Chu, M. Gajek, R. Ramesh, R. Rai, X. Xu, and J. Musfeldt, Photoconductivity in bifeo₃ thin films, *Applied Physics Letters* **92** (2008).
- [13] A. Ghosh, D. P. Trujillo, H. Choi, S. Nakhmanson, S. P. Alpay, and J.-X. Zhu, Electronic and magnetic properties of lanthanum and strontium doped bismuth ferrite: a first-principles study, *Scientific reports* **9**, 194 (2019).
- [14] N. A. Benedek and C. J. Fennie, Hybrid improper ferroelectricity: a mechanism for controllable polarization-magnetization coupling, *Physical review letters* **106**, 107204 (2011).
- [15] P. Gayathri, M. Swamynathan, M. Shaikh, A. Ghosh, and S. Ghosh, Switching of hybrid improper ferroelectricity in oxide double perovskites, *Chemistry of Materials* **35**, 6612 (2023).
- [16] P. Gayathri, S. Ghosh, and A. Ghosh, Predictive design of hybrid improper ferroelectric double perovskite oxides, *Chemistry of Materials* **36**, 682 (2024).
- [17] P. Hohenberg and W. Kohn, Density functional theory (dft), *Phys. Rev* **136**, B864 (1964).
- [18] W. Kohn and L. J. Sham, Self-consistent equations including exchange and correlation effects, *Physical review* **140**, A1133 (1965).
- [19] P. Blaha, K. Schwarz, P. Sorantin, and S. Trickey, Full-potential, linearized augmented plane wave programs for crystalline systems, *Computer physics communications* **59**, 399 (1990).
- [20] J. P. Perdew, K. Burke, and M. Ernzerhof, Generalized gradient approximation made simple, *Physical review letters* **77**, 3865 (1996).
- [21] S. L. Dudarev, G. A. Botton, S. Y. Savrasov, C. Humphreys, and A. P. Sutton, Electron-energy-loss spectra and the structural stability of nickel oxide: An lsd+u study, *Physical Review B* **57**, 1505 (1998).
- [22] F. Tran and P. Blaha, Accurate band gaps of semiconductors and insulators with a semilocal exchange-correlation potential, *Physical review letters* **102**, 226401 (2009).
- [23] S. Buvaneswaran, M. Shaikh, R. Gowsalya, T. Sahoo, and S. Ghosh, Design of ferroelectric double perovskite oxides as photovoltaic materials, *The Journal of Physical Chemistry C* **127**, 15486 (2023).
- [24] S. Buvaneswaran, M. Shaikh, T. Sahoo, and S. Ghosh, Ferroelectric ferrimagnetic double perovskite oxides design for optoelectronics, *Physical Review Materials* **9**, 054401 (2025).
- [25] J. Philipp, P. Majewski, L. Alff, A. Erb, R. Gross, T. Graf, M. Brandt, J. Simon, T. Walther, W. Mader, *et al.*, Structural and doping effects in the half-metallic double perovskite a₂crw₆ (a= sr, ba, and ca), *Physical Review B* **68**, 144431 (2003).
- [26] Y. Tomioka, T. Okuda, Y. Okimoto, R. Kumai, K.-I. Kobayashi, and Y. Tokura, Magnetic and electronic properties of a single crystal of ordered double perovskite sr₂femoo₆, *Physical Review B* **61**, 422 (2000).
- [27] K.-I. Kobayashi, T. Kimura, H. Sawada, K. Terakura, and Y. Tokura, Room-temperature magnetoresistance in an oxide material with an ordered double-perovskite structure, *Nature* **395**, 677 (1998).
- [28] D. Sarma, A new class of magnetic materials: Sr₂femoo₆ and related compounds, *Current Opinion in Solid State and Materials Science* **5**, 261 (2001).
- [29] P. A. Kumar, R. Mathieu, R. Vijayaraghavan, S. Majumdar, O. Karis, P. Nordblad, B. Sanyal, O. Eriksson, and

- D. D. Sarma, Ferrimagnetism, antiferromagnetism, and magnetic frustration in $\text{La}_{2-x}\text{Sr}_x\text{CuO}_6$ ($0 \leq x \leq 1$), *Physical Review B—Condensed Matter and Materials Physics* **86**, 094421 (2012).
- [30] D. Sarma and S. Ray, Properties of a new magnetic material: $\text{Sr}_2\text{FeMoO}_6$, *Journal of Chemical Sciences* **113**, 515 (2001).
- [31] S. Ray, A. Kumar, D. Sarma, R. Cimino, S. Turchini, S. Zenaro, and N. Zema, Electronic and magnetic structures of $\text{Sr}_2\text{FeMoO}_6$, *Physical Review Letters* **87**, 097204 (2001).
- [32] See Supplemental Material at [URL will be inserted by publisher].
- [33] M. Shaikh, A. Fathima, M. Swamynadhan, H. Das, and S. Ghosh, Investigation into cation-ordered magnetic polar double perovskite oxides, *Chemistry of Materials* **33**, 1594 (2021).
- [34] A. Zunger, S.-H. Wei, L. Ferreira, and J. E. Bernard, Special quasirandom structures, *Physical review letters* **65**, 353 (1990).
- [35] R. King-Smith and D. Vanderbilt, Theory of polarization of crystalline solids, *Physical Review B* **47**, 1651 (1993).
- [36] M. B. Johnston and L. M. Herz, Hybrid perovskites for photovoltaics: charge-carrier recombination, diffusion, and radiative efficiencies, *Accounts of chemical research* **49**, 146 (2016).
- [37] J.-Y. Wu, X. Jin, J. Wang, Z. Hu, C.-Y. Chen, T. Kurioka, J. Llandro, A. H. Gibbons, M. Sone, Y.-J. Hsu, *et al.*, Enhancement of photocatalytic activity in BiFeO_3 nanoparticles through electrical polarization, *Advanced Energy and Sustainability Research*, 2400285 (2025).
- [38] M. Kato, M. Nishiwaki, and H. Fujiwara, Very high oscillator strength in the band-edge light absorption of zincblende, chalcopyrite, kesterite, and hybrid perovskite solar cell materials, *Physical Review Materials* **4**, 035402 (2020).
- [39] E. M. Chen, L. Williams, A. Olvera, C. Zhang, M. Zhang, G. Shi, J. T. Heron, L. Qi, L. J. Guo, E. Kioupakis, *et al.*, Sustainable p-type copper selenide solar material with ultra-large absorption coefficient, *Chemical Science* **9**, 5405 (2018).
- [40] M. Shirayama, H. Kadowaki, T. Miyadera, T. Sugita, M. Tamakoshi, M. Kato, T. Fujiseki, D. Murata, S. Hara, T. N. Murakami, *et al.*, Optical transitions in hybrid perovskite solar cells: ellipsometry, density functional theory, and quantum efficiency analyses for $\text{CH}_3\text{NH}_3\text{PbI}_3$, *Physical Review Applied* **5**, 014012 (2016).
- [41] P. Brody and B. Rod, Decay of remanent polarization in ferroelectric films using polarization-dependent photovoltages, *Integrated Ferroelectrics* **3**, 245 (1993).
- [42] A. T. Mulder, N. A. Benedek, J. M. Rondinelli, and C. J. Fennie, Turning ABO_3 antiferroelectrics into ferroelectrics: design rules for practical rotation-driven ferroelectricity in double perovskites and $\text{A}_3\text{B}_2\text{O}_7$ Ruddlesden-Popper compounds, *Advanced Functional Materials* **23**, 4810 (2013).
- [43] H. L. Feng, M. Arai, Y. Matsushita, Y. Tsujimoto, Y. Guo, C. I. Sathish, X. Wang, Y.-H. Yuan, M. Tanaka, and K. Yamaura, High-temperature ferrimagnetism driven by lattice distortion in double perovskite Ca_2FeO_6 , *Journal of the American Chemical Society* **136**, 3326 (2014).
- [44] Z. Zanolli, J. C. Wojdeł, J. Íñiguez, and P. Ghosez, Electric control of the magnetization in $\text{BiFeO}_3/\text{LaFeO}_3$ superlattices, *Physical Review B—Condensed Matter and Materials Physics* **88**, 060102 (2013).